

IDEA: An Inverse Domain Expert Adaptation Based Active DNN IP Protection Method

Chaohui Xu, Qi Cui, Jinxin Dong, Weiyang He, and Chip-Hong Chang

Abstract—Illegitimate reproduction, distribution and derivation of Deep Neural Network (DNN) models can inflict economic loss, reputation damage and even privacy infringement. Passive DNN intellectual property (IP) protection methods such as watermarking and fingerprinting attempt to prove the ownership upon IP violation, but they are often too late to stop catastrophic damage of IP abuse and too feeble against strong adversaries. In this paper, we propose IDEA, an Inverse Domain Expert Adaptation based proactive DNN IP protection method featuring active authorization and source traceability. IDEA generalizes active authorization as an inverse problem of domain adaptation. The multi-adaptive optimization is solved by a mixture-of-experts model with one real and two fake experts. The real expert re-optimizes the source model to correctly classify test images with a unique model user key steganographically embedded. The fake experts are trained to output random prediction on test images without or with incorrect user key embedded by minimizing their mutual information (MI) with the real expert. The MoE model is knowledge distilled into a unified protected model to avoid leaking the expert model features by maximizing their MI with additional multi-layer attention and contrastive representation loss optimization. IDEA not only prevents unauthorized users without the valid key to access the functional model, but also enable the model owner to validate the deployed model and trace the source of IP infringement. We extensively evaluate IDEA on five datasets and four DNN models to demonstrate its effectiveness in authorization control, culprit tracing success rate, and robustness against various attacks.

Index Terms—Deep neural networks, IP protection, mixture-of-experts, knowledge distillation, domain adaptation.

I. INTRODUCTION

The past decade has witnessed proliferate applications of DNNs in almost every sector of business. Building a high-performance DNN requires significant data collection and labeling effort, computing resources, and expert knowledge. These painstakingly trained models are alluring targets of piracy and misappropriation. When a trained DNN is directly distributed to the end users, the internal structure and parameters of the deployed model can be easily duplicated by rival adversaries or dishonest consumers with full access to the model. Even if the trained model is deployed on the cloud to remote endpoint users for online inference through application program interface (API), recent studies [1]–[5] demonstrated that a surrogate model can be trained to achieve comparable performance as the source model at a substantially reduced cost than designing the model from scratch.

In view of the rampant DNN intellectual property (IP) theft, various protection methods have been proposed in recent years. The approaches can be categorized into passive and active protection methods. Passive protection methods, such as watermarking [6]–[12] and fingerprinting [13]–[16], aim

at detecting the ownership of the deployed DNN upon IP infringement, whereas active protection methods, such as [17]–[21], aim at preventing IP violation proactively. The latter limits unauthorized users without a valid key from accessing the full utility of the deployed model by multi-task optimization. Constrained by multiple optimization objectives, these optimization techniques mainly alter the decision boundaries of the last and/or penultimate layers. As the feature distribution in the shallow layers remains almost identical for both authorized and unauthorized samples, they can be easily exploited for successful fine-tuning attacks.

In this paper, we propose IDEA – an active DNN IP protection method based on Inverse Domain Expert Adaptation. It enables the owner to proactively lock the model’s functionality from access by unauthorized users without a valid user key. Even if the model has been misappropriated, the owner can still claim the ownership and trace the culprit responsible for the model leakage. Our novel contributions are as follows. Unlike existing methods, IDEA treats the active authorization IP protection as an inverse problem of domain adaptation and solves it by training a mixture of experts (MoE) to minimize the mutual information (MI) between the authorized source and unauthorized target domains. A real expert is fine-tuned from the unprotected model to produce accurate prediction on authorized images. Authorized images can be produced by hiding a user key using a trained invertible Steganographic Generative Adversarial Network (SteganoGAN). The encoder of the SteganoGAN is distributed to legitimate users while the decoder is kept private by the model owner for user tracking. Two fake experts are trained to intentionally degrade the prediction accuracy on unencoded clean images and images encoded with invalid key, respectively. The three independently trained experts are inseparably fused into a coherent protected model by knowledge distillation across several selected hidden layers from shallow to depth. The stealthiness, effectiveness, fidelity and uniqueness of IDEA are evaluated by extensive experiments across five popular datasets and four network architectures. Its superiority over existing active protection methods and robustness against a wide range of attacks have also been validated.

The rest of the paper is organized as follows. Related works are reviewed in Section II. Our threat model and problem formulation, background knowledge on SteganoGAN and domain expected risk bound are presented in Section III. The proposed IDEA is elaborated in Section IV. Section V presents the experimental results and comparison, followed by the latent representations visualization and security analysis in Sections VI and VII, respectively. The paper is concluded in

Section VIII.

II. RELATED WORKS

A. *Passive Protection*

DNN watermarking is a passive means of IP rights protection by concealing the copyright information into the target model. In the event of IP piracy, the embedded information can be extracted to prove the ownership. The first DNN watermarking method [6] embeds secret information into the model’s weights by including an additional regularization loss during training and constraining the biases of the embedded hidden layers to follow a particular distribution. To enhance the watermark robustness against colluded modifications by malicious users, DeepMark [10] assigns each user a unique fingerprint using anti-collusion codebook and retrains the model with a fingerprint-specific regularization loss. To avoid accuracy degradation in black-box watermarking, RIGA [11] uses adversarial training to increase the covertness and robustness against watermark removal but white-box access is needed for watermark verification. To facilitate ownership verification by querying the model remotely via the API, adversarial examples [7] are used to tweak the decision boundaries for watermark embedding. For better transferability across various model architectures, the model is watermarked by backdoor-ing [8]. The watermarking framework is generalized in [22] to support both black-box and white-box accesses by leveraging meaningful content, unrelated content, and meaningless noise for backdoor trigger generation.

In contrast, DNN fingerprinting methods extract unique intrinsic characteristics of the model for ownership proof without modifying the pretrained model. PoL [13] creates a unique fingerprint from specific details of the training process. IP-Guard [14] utilizes adversarial examples while ModelDiff [15] exploits the model’s decision distance vectors to characterize and identify the decision boundary for unique fingerprint construction. Both methods allow remote black-box ownership verification through the APIs. More recently, a transfer learnt resilient fingerprint [16] is proposed by projecting selected weights from the front layers of the victim model to the random space generated by the owner’s notary identity.

B. *Active Protection*

Active protection methods control the model usage by allowing the full functionality of the model to be accessible by only authorized users. Our method falls into this category.

HPNN [17] embeds the encoded model into a trustworthy hardware device. In [18], the model is trained on pixel-shuffled samples to attain optimal inference performance exclusively on test samples that have been shuffled with the same secret key. ChaoWs [20] rearranges the neuron positions to encrypt a trained model, which can only be decrypted with the secret key provided by the owner. M-LOCK [23] and SSAT [21] trains the model with correctly labeled trigger-embedded training samples and wrongly labeled clean training samples so that the trained model can only accurately classify images with the pre-defined backdoor trigger. DSN [24] pastes a binary pattern trigger on training images, and utilizes a gradient reversal

layer [25] to train the protected model to behave differently on images with and without the trigger. NTL [26] restricts the model’s generalization ability to a certain domain to realize active authorization.

DeepIPR [19] is the first passport-based protection scheme for access control and ownership verification. This method replaces selected normalization layers of the model with passport layers to degrade its performance. Authorized users can restore the model’s original performance by submitting a valid passport image along with the test images. PAN [27] jointly trains the target model with a passport-aware branch to avoid model structure modification; however, this method lacks the usage control in the distributed passport-free branch. TdN [28] enables irreversible ownership verification against ambiguity attacks with oracle passports. Recently, Steganographic passport [29] hides the user’s identity images into the passport with an invertible steganographic network. This approach offers robust ownership proof without necessitating extra model retraining for each new user.

C. *Domain Adaption*

Domain adaptation aims to improve the generalizability of a DNN model from the source domain to other related target domains with access to the target training data. Many existing domain adaptation approaches align domain distributions by minimizing the measured distance between domains, such as maximum mean discrepancy (MMD), correlation alignment (CORAL) [30], and contrastive domain discrepancy (CDD) [31]. Some approaches utilize neural networks, like autoencoders or adversarial-based networks [32], to diminish the domain gap by decreasing the discrepancy between feature representations in the hidden layers.

III. PRELIMINARIES

A. *Threat Model*

Under the active protection paradigm, the defender is assumed to have complete knowledge and control over all components and training pipelines of a model before it is distributed and deployed. As the adversary can be a legal buyer who illegally redeploys the purchased model for profit beyond the contracted term, the protected model’s parameters and architecture are assumed to be transparent to the adversaries. During the verification stage, the defender can only query the suspected model with a few reserved test samples. The outputs can be analyzed to determine if it is a counterfeit copy, and trace the source of counterfeit if it is.

B. *Problem Formulation*

We formulate the active authorization as an inverse problem of domain adaptation. Our goal is to maintain a high inference accuracy of the protected model on the authorized (source) domain, where the input data are embedded with the correct key, while weakening its generalizability on unauthorized

(target) domains with missing or incorrect keys. Given a pre-trained encoder $\mathcal{E}(\cdot, \cdot)$ and a binary key $k_j \in \mathcal{K}$, the following three domains of input samples can be defined.

$$\mathcal{B} = \left\{ (x, y) \mid x \sim \mathcal{P}_X^{\mathcal{B}}, y \sim \mathcal{P}_Y^{\mathcal{B}} \right\}, \quad (1)$$

$$\mathcal{A}_j = \left\{ (x_j^+, y) \mid x_j^+ := \mathcal{E}(x, k_j), x_j^+ \sim \mathcal{P}_X^{\mathcal{A}_j}, y \sim \mathcal{P}_Y^{\mathcal{A}_j} \right\}, \quad (2)$$

$$\mathcal{N}_j = \left\{ (x_j^-, y) \mid x_j^- := \mathcal{E}(x, k^*), x_j^- \sim \mathcal{P}_X^{\mathcal{N}_j}, y \sim \mathcal{P}_Y^{\mathcal{N}_j} \right\}. \quad (3)$$

The benign domain \mathcal{B} consists of the original samples, where $\mathcal{P}_X^{\mathcal{B}}$ and $\mathcal{P}_Y^{\mathcal{B}}$ denote the distributions of benign images and labels, respectively. The authorized domain \mathcal{A}_j contains authorized samples that are all embedded with the correct key k_j . The noise domain \mathcal{N}_j contains samples that are each embedded with a different random wrong key $k^* \neq k_j$.

We consider a K -class image classifier $f_\theta(\cdot)$ trained on the training dataset $D_{\text{tr}} = \{(x_i, y_i)\}_{i=1}^{N_{\text{tr}}}$, with θ being the trained parameters. Instead of directly releasing the unprotected model $f_\theta(\cdot)$ to M paying customers, the model owner further generates M different protected models $\{f_{\theta_1}(\cdot), f_{\theta_2}(\cdot), \dots, f_{\theta_M}(\cdot)\}$ from $f_\theta(\cdot)$ by embedding into each instance one of the M unique user-specific keys $\mathcal{K} = \{k_1, k_2, \dots, k_M\}$. Each protected model has special prediction behaviors on input samples from different domains.

Definition 1 (Key-based Active Authorization). *Given the benign domain \mathcal{B} , a specific binary key k_j , and the corresponding authorized and noise domains \mathcal{A}_j and \mathcal{N}_j , respectively. A model $f_{\theta_j}(\cdot)$ protected by the key-based active authorization is a k_j encoded instance derived from an unprotected model $f_\theta(\cdot)$ to perform well only on \mathcal{A}_j but predicts randomized outputs on \mathcal{B} and \mathcal{N}_j like a untrained model. The protected model fulfills the following three properties:*

$$\mathbb{E}_{(x,y) \sim \mathcal{B}} [\mathbb{I}\{f_\theta(x) = y\}] - \mathbb{E}_{(x_j^+, y) \sim \mathcal{A}_j} [\mathbb{I}\{f_{\theta_j}(x_j^+) = y\}] < \epsilon_1, \quad (4)$$

$$\mathbb{E}_{(x,y) \sim \mathcal{B}} [\mathbb{I}\{f_\theta(x) = y\}] - \mathbb{E}_{(x,y) \sim \mathcal{B}} [\mathbb{I}\{f_{\theta_j}(x) = y\}] > \epsilon_2, \quad (5)$$

$$\mathbb{E}_{(x,y) \sim \mathcal{B}} [\mathbb{I}\{f_\theta(x) = y\}] - \mathbb{E}_{(x_j^-, y) \sim \mathcal{N}_j} [\mathbb{I}\{f_{\theta_j}(x_j^-) = y\}] > \epsilon_2, \quad (6)$$

where $\mathbb{E}_{(x,y) \sim \mathcal{B}} [\mathbb{I}\{f_\theta(x) = y\}]$ represents the accuracy of the unprotected model evaluated on the benign domain. ϵ_1 and ϵ_2 denote two positive fractions that set the accuracy preservation and degradation thresholds, respectively.

Eq. (4) specifies the **fidelity** requirement on authorized access, which requires the protected model $f_{\theta_j}(\cdot)$ to guarantee performance of no more than a trivial accuracy drop from $f_\theta(\cdot)$ on images encoded with the correct key k_j . Eq. (5) stipulates the **effectiveness** against unauthorized access, which requires the accuracy of $f_{\theta_j}(\cdot)$ to fall below that of the original model by a substantial margin in the absence of a valid key k_j . Eq. (6) specifies the **uniqueness** criterion, which calls for a unique key to affiliate with each encoded model instance. Mismatched model-key pairs will result in a substantial accuracy degradation from its source model.

Each model-key pair (i.e., $\{f_{\theta_j}(\cdot), k_j\}$) along with the unified encoder $\mathcal{E}(\cdot, \cdot)$ are distributed to the corresponding legal user. Given only black-box access to a suspected model $f_{\theta'}(\cdot)$, the following definition supports ownership verification and dishonest user identification.

Definition 2 (Ownership Verification). *Let D_q denotes a benign query set sampled from the benign domain, the own-*

ership of the model owner over the suspected model $f_{\theta'}(\cdot)$ is verified if $\exists! k_j \in \mathcal{K}$ fulfills:

$$\mathbb{E}_{(x,y) \sim D_q} |\mathbb{I}\{f_\theta(x) = y\} - \mathbb{I}\{f_{\theta'}(\mathcal{E}(x, k_j)) = y\}| < \epsilon_1, \quad (7)$$

$$\mathbb{E}_{(x,y) \sim D_q} |\mathbb{I}\{f_{\theta'}(x) = y\} - \mathbb{I}\{f_{\theta'}(\mathcal{E}(x, k_j)) = y\}| > \epsilon_2. \quad (8)$$

Eq. (7) proves that the full functionality of the suspected model can be activated by a recorded key, and Eq. (8) rules out its possibility as an innocent model. The user who is assigned the traced key k_j can be determined from the illegally resold or redistributed model.

C. SteganoGAN

SteganoGAN [33] is a lightweight steganographic network for key encoding and decoding. It consists of three sub-networks: the encoder $\mathcal{E}(\cdot, \cdot)$, the decoder $\mathcal{D}(\cdot)$, and the critic $\mathcal{C}(\cdot)$. The training loss of the encoder-decoder network is composed of three losses, \mathcal{L}_d , \mathcal{L}_s and \mathcal{L}_r :

$$\mathcal{L}_d = \mathbb{E}_{x \sim \mathcal{P}_C} [\mathcal{L}_{\text{BCE}}(\mathcal{D}(\mathcal{E}(x, \text{msg}), \text{msg}))], \quad (9)$$

$$\mathcal{L}_s = \mathbb{E}_{x \sim \mathcal{P}_C} [\mathcal{L}_{\text{MSE}}(x - \mathcal{E}(x, \text{msg}))], \quad (10)$$

$$\mathcal{L}_r = \mathbb{E}_{x \sim \mathcal{P}_C} [\mathcal{C}(\mathcal{E}(x, \text{msg}))], \quad (11)$$

where \mathcal{P}_C denotes the training set of SteganoGAN, \mathcal{L}_{BCE} and \mathcal{L}_{MSE} represent the binary cross-entropy loss and mean square error loss, respectively. msg is an encoded or a decoded binary message that has the same dimension as the cover image x . The decoding loss \mathcal{L}_d ensures that the encoded message can be accurately extracted from the stego image; the similarity loss \mathcal{L}_s forces the stego image to resemble the cover image; and the realness loss \mathcal{L}_r mitigates distortion in the stego image.

D. Domain Expected Risk Bound

Given the source domain \mathcal{S} and a target domain \mathcal{T} of a DNN classifier f , the expected risk on the source and target domains can be represented as $\mathcal{R}_{\mathcal{S}}(f) = \mathbb{E}_{(x,y) \sim \mathcal{S}} [\mathbb{I}\{f(x) \neq y\}]$ and $\mathcal{R}_{\mathcal{T}}(f) = \mathbb{E}_{(\hat{x}, y) \sim \mathcal{T}} [\mathbb{I}\{f(\hat{x}) \neq y\}]$, respectively. The expected risk on the target domain is upper bounded by the latent features as follows [34]:

$$\begin{aligned} \mathcal{R}_{\mathcal{T}}(f) &\leq \mathcal{R}_{\mathcal{S}}(f) - 4I(z; \hat{z}) \\ &\quad + 4H(Y) + \frac{1}{2}d_{\mathcal{H}\Delta\mathcal{H}}(p(z), p(\hat{z})), \end{aligned} \quad (12)$$

where z and \hat{z} represent the latent features extracted independently from the same hidden layer on the source and target domains, respectively. $I(z; \hat{z})$ represents the MI between the latent features. $H(Y)$ is the entropy of label distribution. $d_{\mathcal{H}\Delta\mathcal{H}}(p(z), p(\hat{z}))$ is the $\mathcal{H}\Delta\mathcal{H}$ -divergence [34] between the source and target domain feature marginal distributions.

Depredating the generalization performance on \mathcal{T} requires the expected risk $\mathcal{R}_{\mathcal{T}}(f)$ to increase. For domain adaptation [34], [35], it is sufficient to increase the expected risk on \mathcal{T} by only minimizing the upper bound of MI between z and \hat{z} , $I(z; \hat{z})$. This upper bound can be determined by the Contrastive Log-ratio Upper Bound (CLUB) [36] as follows:

$$\begin{aligned} I(z; \hat{z}) &= \mathbb{E}_{p(z, \hat{z})} \left[\log \frac{p(z, \hat{z})}{p(z)p(\hat{z})} \right] \leq I_{\text{CLUB}}(z; \hat{z}) \\ &= \mathbb{E}_{p(z, \hat{z})} [\log p(\hat{z}|z)] - \mathbb{E}_{p(z)p(\hat{z})} [\log p(\hat{z}|z)], \end{aligned} \quad (13)$$

where $p(z, \hat{z})$ denotes the joint probability distribution of z and \hat{z} .

The unknown conditional distribution $p(\hat{z}|z)$ can be approximated by the variational distribution $q_\phi(\hat{z}|z)$ with an auxiliary

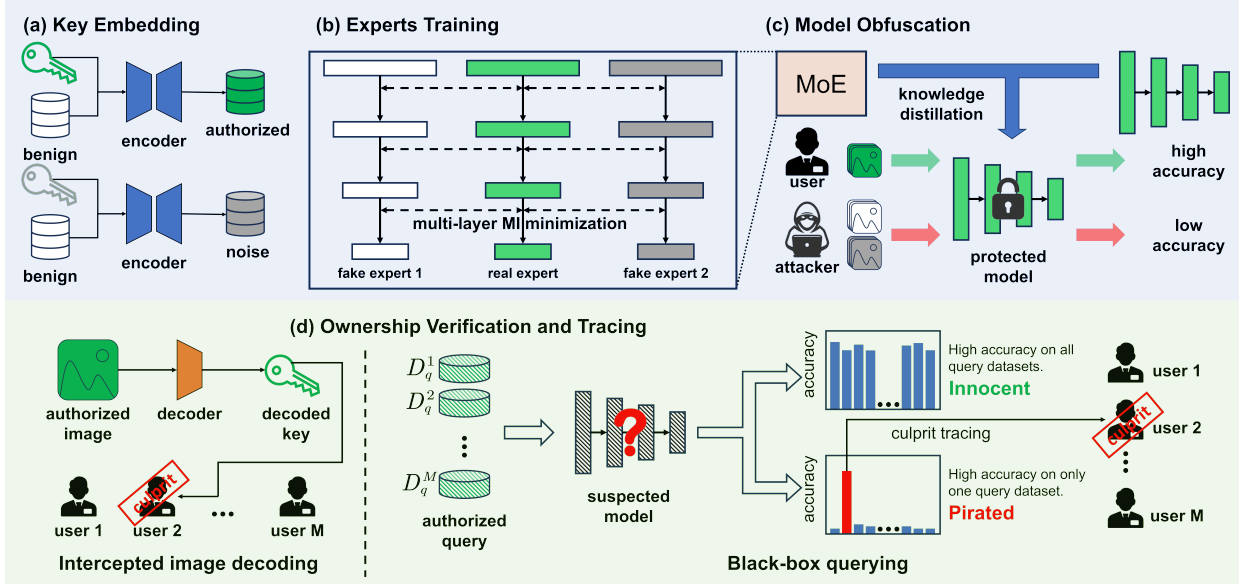


Fig. 1: Overall pipeline of IDEA, a solution to the inverse problem of domain adaptation for key-based active authorization.

neural network parameterized with ϕ [36]. By feeding samples $\{(z_i, \hat{z}_i)\}_{i=1}^{N_{\text{est}}}$ into the auxiliary network,

$$\hat{I}(z; \hat{z}) = \frac{1}{N_{\text{est}}} \sum_{m=1}^{N_{\text{est}}} \left[\log q_{\phi}(\hat{z}_m | z_m) - \frac{1}{N_{\text{est}}} \sum_{n=1}^{N_{\text{est}}} \log q_{\phi}(\hat{z}_n | z_m) \right]. \quad (14)$$

A DNN classifier f of L layers can be expressed as $f = f_1 \circ f_2 \circ \dots \circ f_L$. The activation output of the l -th layer is denoted as $f^l \in \mathbb{R}^{c_l \times h_l \times w_l}$, where c_l , h_l and w_l denote the dimensions of channel, height and width, respectively of the activation map. Previous works [26], [35] focused on minimizing the MI between the latent features output by the penultimate layer (i.e., f_{L-1}) to reduce the generalization of \mathcal{T} . We observe that the source and target domain samples share minimal information at the penultimate layer. Their latent features in the earlier layers are fairly similar, which can leak vital information about the protected model's functionality. To avoid this vulnerability, we jointly minimize the MI between \mathcal{S} and \mathcal{T} on 4 selected hidden layers that are evenly distributed from shallow to deep within the model, i.e.,

$$\min_{l \in T_{\text{sel}}} \sum \hat{I}(f^l; \hat{f}^l), \quad \text{where } T_{\text{sel}} = \{l_1, l_2, l_3, l_4\}. \quad (15)$$

IV. THE PROPOSED METHOD

Fig. 1 illustrates the overall pipeline of our proposed method. It consists of three steps: key embedding, experts training, and model obfuscation.

A. Key Embedding

Fig. 2 shows an example of key encoding and decoding. Each individual user is assigned a unique key $k_j \in \{0, 1\}^{c \times r \times r}$, which is a binary square matrix derived from the identity of a user, where c is the number of channels and r denotes the length of the square matrix. The entire key space \mathcal{K} is $2^{c \times r \times r}$. Notably, r is much smaller than the height h and width w of the original image $x \in [0, 1]^{3 \times h \times w}$. To match the sizes of k_j and x , we concatenate multiple non-overlapping blocks of k_j to obtain the expanded key $\text{Exp}(k_j) \in \{0, 1\}^{c \times h \times w}$. The encoded image $x_j = \mathcal{E}(x, \text{Exp}(k_j))$ is generated by simultaneously feeding x_i and $\text{Exp}(k_j)$ into the encoder. During the

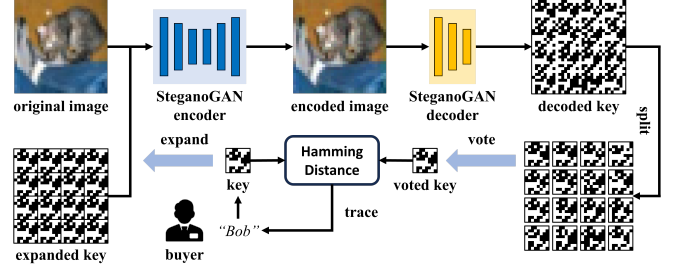


Fig. 2: Key embedding into a cover image by the pretrained SteganoGAN encoder and key extraction from the stego image by the model owner with the corresponding pretrained SteganoGAN decoder (private). The SteganoGAN encoder and decoder are pre-trained on the original training dataset D_{tr} .

verification stage, x_j is passed through the decoder $\mathcal{D}(\cdot)$ and split into multiple non-overlapping blocks of size $r \times r$. A majority voting process is then conducted across corresponding elements of all blocks to extract the key \hat{k}_j . This operation can be formally expressed as $\hat{k}_j = \text{Vote}(\text{Split}(\mathcal{D}(x_j)))$.

The encoder is distributed to all authorized users for embedding their unique user keys into the test images. The decoder is kept private and reserved for the model owner to recover the embedded user key in any encoded test images. The perturbations introduced by the encoder into the images are visually imperceptible and sample-specific, i.e., the perturbations due to the same embedded key vary across images.

B. Experts Training

Let \mathcal{A}_j be the source domain, and \mathcal{B} and \mathcal{N}_j be two different target domains. An inverse problem of domain adaption can be solved by optimizing the domain expected risk bound in Sec. III-D to maintain the good performance of the authorized source domain and reduce the generalization of the unauthorized target domains. To fulfill **Definition 1**, the training objective of the protected model $f_{\theta_j}(\cdot)$ can be formulated as

a bi-level optimization problem as follows:

$$\begin{aligned}
& \arg \min_{\theta_j} \mathbb{E}_{(x_j^+, y) \sim \mathcal{A}_j} \left[\mathcal{L}_{\text{CE}} \left(f_{\theta_j}(x_j^+), y \right) \right] \\
& + \lambda_3 \sum_{l \in T_{\text{sel}}} \mathbb{E}_{p(x_j^+, x)} \left[\hat{I} \left(f_{\theta_j}^l(x_j^+); f_{\theta_j}^l(x) \right) \right] \\
& + \lambda_3 \sum_{l \in T_{\text{sel}}} \mathbb{E}_{p(x_j^+, x_j^-)} \left[\hat{I} \left(f_{\theta_j}^l(x_j^+); f_{\theta_j}^l(x_j^-) \right) \right], \quad (16) \\
& \text{s.t. } \phi_1^l = \arg \min_{\phi_1} \mathbb{E}_{p(x_j^+, x)} \left[\hat{I} \left(f_{\theta_j}^l(x_j^+); f_{\theta_j}^l(x) \right) \right], \\
& \phi_2^l = \arg \min_{\phi_2} \mathbb{E}_{p(x_j^+, x_j^-)} \left[\hat{I} \left(f_{\theta_j}^l(x_j^+); f_{\theta_j}^l(x_j^-) \right) \right],
\end{aligned}$$

where $f_{\theta_j}^l(x)$, $f_{\theta_j}^l(x_j^+)$ and $f_{\theta_j}^l(x_j^-)$ denote the l -th layer latent features of \mathcal{B} , \mathcal{A}_j and \mathcal{N}_j domains, respectively. ϕ_1^l and ϕ_2^l are parameters of the two auxiliary networks used to estimate the l -th layer MI between the source domain and two target domains, i.e., $\hat{I}(f_{\theta_j}^l(x_j^+); f_{\theta_j}^l(x))$ and $\hat{I}(f_{\theta_j}^l(x_j^+); f_{\theta_j}^l(x_j^-))$. λ_3 is a factor to balance the contributions of different terms.

Unfortunately, it is computationally intensive to iteratively update the two auxiliary networks in tandem with the protected model. Moreover, the optimization of Eq. (16) is difficult to converge. The trained model often exhibits polarized behavior, consistently classifying test images either correctly (satisfying the first term) or incorrectly (satisfying the last two terms), regardless of whether the images are authorized. To address these issues, we design an MoE [37] model $\mathcal{M}_j(\cdot)$ with three components: one real expert model $f_{\theta_j^R}(\cdot)$ that performs well on \mathcal{A}_j , and two fake expert models $f_{\theta_j^{F1}}(\cdot)$ and $f_{\theta_j^{F2}}(\cdot)$ to compromise the performance on two unauthorized domains \mathcal{B} and \mathcal{N}_j , respectively. The real expert model can be fine-tuned from the unprotected benign model $f_{\theta}(\cdot)$ for a few epochs to ensure it achieves the optimal performance on \mathcal{A}_j by optimizing

$$\hat{\theta}_j^R = \arg \min_{\theta_j^R} \mathbb{E}_{(x_j^+, y) \sim \mathcal{A}_j} \left[\mathcal{L}_{\text{CE}} \left(f_{\theta_j^R}(x_j^+), y \right) \right]. \quad (17)$$

Conversely, the two fake experts are separately optimized by minimizing their MI with the real expert $f_{\theta_j^R}(\cdot)$ in selected layers as follows:

$$\hat{\theta}_j^{F1} = \arg \min_{\theta_j^{F1}} \sum_{l \in T_{\text{sel}}} \mathbb{E}_{p(x_j^+, x)} \left[\hat{I} \left(f_{\theta_j^R}^l(x_j^+), f_{\theta_j^{F1}}^l(x) \right) \right], \quad (18)$$

$$\hat{\theta}_j^{F2} = \arg \min_{\theta_j^{F2}} \sum_{l \in T_{\text{sel}}} \mathbb{E}_{p(x_j^+, x_j^-)} \left[\hat{I} \left(f_{\theta_j^R}^l(x_j^+), f_{\theta_j^{F2}}^l(x_j^-) \right) \right]. \quad (19)$$

The training objective of Eq. (16) is decomposed into three terms independently optimized by Eqs. (17) (18) and (19) in three separate models. Since the three optimization terms are now disentangled from each other, the training process of the three experts can converge more quickly, thereby reducing the training cost. The trained MoE model $\mathcal{M}_j(\cdot)$ can be expressed as follows:

$$\mathcal{M}_j(x) = \begin{cases} f_{\theta_j^R}(x), & \text{if } x \sim \mathcal{A}_j, \\ f_{\theta_j^{F1}}(x), & \text{if } x \sim \mathcal{B}, \\ f_{\theta_j^{F2}}(x), & \text{if } x \sim \mathcal{N}_j. \end{cases} \quad (20)$$

We separately feed 1500 paired test images sampled from $\mathcal{W} = \mathcal{A}_j \cup \mathcal{B} \cup \mathcal{N}_j$ (i.e., 500 samples for each subdomain) and visualize their latent features with t-distributed Stochastic Neighbor Embedding (t-SNE) technique [38]. As shown in Fig. 3, the latent features form three distinct clusters corresponding to their respective subdomains. As expected, the authorized domain shares minimal MI with the two unauthorized

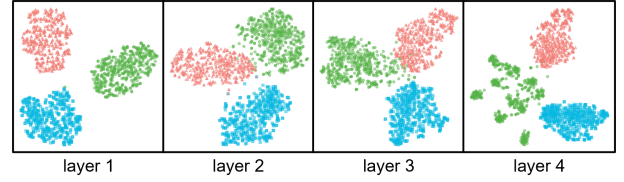


Fig. 3: The t-SNE visualization [38] of latent outputs of the selected layers of MoE model to paired test images. The **blue**, **green**, and **red** data points denote the latent representations of benign, authorized, and noise images, respectively.

domains in the latent space. Consequently, the latent features from different domains exhibit increased separation.

C. Model Obfuscation

It is worth noting that the MoE model $\mathcal{M}_j(\cdot)$ lacks a gating network to decide which expert should be activated for prediction. Consequently, $\mathcal{M}_j(\cdot)$ requires prior knowledge about the domain from which the input image is sampled to activate the correct domain expert, which is impractical in real-world scenarios. Additionally, distributing $\mathcal{M}_j(\cdot)$ directly to a user poses a security risk, as adversaries can easily identify the real expert due to its superior classification performance on benign test samples compared to the two fake experts. To address these issues, we obfuscate the three experts by unifying them into a single coherent model using knowledge distillation. We use $\mathcal{M}_j(\cdot)$ to train a student model $f_{\theta_j^p}(\cdot)$ with the secret key k_j for distributing to an authorized user. We want $f_{\theta_j^p}(\cdot)$ to imitate the teacher's behaviors over \mathcal{W} on not only the fully-connected layer but all selected hidden layers from shallow to deep. To achieve this, we jointly optimize $f_{\theta_j^p}(\cdot)$ with three knowledge distillation losses \mathcal{L}_{kl} , \mathcal{L}_{at} and \mathcal{L}_{crd} such that

$$\hat{\theta}_j^p = \arg \min_{\theta_j^p} [\mathcal{L}_{\text{kl}} + \lambda_1 \mathcal{L}_{\text{at}} + \lambda_2 \mathcal{L}_{\text{crd}}], \quad (21)$$

where λ_1 and λ_2 are two positive factors to adjust the scale of \mathcal{L}_{at} and \mathcal{L}_{crd} , respectively.

(1) Minimizing \mathcal{L}_{kl} aligns the logits output by the fully connected layers of the teacher and student models. \mathcal{L}_{kl} can be computed as:

$$\mathcal{L}_{\text{kl}} = \mathbb{E}_{x \sim \mathcal{W}} \left[\mathcal{L}_{\text{KL}} \left(f_{\theta_j^p}(x), \mathcal{M}_j(x) \right) \right] \quad (22)$$

where \mathcal{L}_{KL} denotes the Kullback-Leibler (KL) divergence between two distributions.

(2) A 3D feature map $f^l \in \mathbb{R}^{c_l \times h_l \times w_l}$ can be flattened along the channel dimension by the attention operator $\mathcal{A}^\alpha(\cdot)$:

$$\mathcal{A}^\alpha(f^l) = \sum_{i=1}^{c_l} |f_i^l|^\alpha, \quad (23)$$

where $\alpha > 1$ is the factor that amplifies large neuron activations. Enlarging α places greater emphasis on regions with high output values. α is fixed to 2 according to [39].

The attention transfer loss [40] is computed as:

$$\mathcal{L}_{\text{AT}}(f_T^l, f_S^l) = \left\| \frac{\mathcal{A}^\alpha(f_T^l)}{\|\mathcal{A}^\alpha(f_T^l)\|_2} - \frac{\mathcal{A}^\alpha(f_S^l)}{\|\mathcal{A}^\alpha(f_S^l)\|_2} \right\|_2, \quad (24)$$

where f_T^l and f_S^l represent the features extracted from the teacher and student models at the l -th layer, respectively.

Algorithm 1: Encoded Model Generation

Input: Benign training dataset D_{tr} ; unprotected model $f_{\theta}(\cdot)$; SteganoGAN encoder $\mathcal{E}(\cdot, \cdot)$; M unique user keys $\mathcal{K} = \{k_1, k_2, \dots, k_M\}$; training epochs $\{E_1, E_2, E_3\}$; learning rates $\{\eta_1, \eta_2, \eta_3\}$; set of selected hidden layers T_{sel} .

Output: M specifically-encoded models $\{f_{\theta_1^p}(\cdot), f_{\theta_2^p}(\cdot), \dots, f_{\theta_M^p}(\cdot)\}$.

- 1 **for** $k_j \in \{k_1, k_2, \dots, k_M\}$ **do**
- 2 **# Generate the authorized and noise training datasets**
- 3 $D_{tr,j}^+ \leftarrow \{(\mathcal{E}(x_i, k_j), y_i)\}_{i=1}^{N_{tr}}$
- 4 $D_{tr,j}^- \leftarrow \{(\mathcal{E}(x_i, k^*), y_i)\}_{i=1}^{N_{tr}}$
- 5 $\bar{D}_{tr,j} = D_{tr} + D_{tr,j}^+ + D_{tr,j}^-$
- 6 **# Experts training**
- 7 Fine-tune the real expert model for E_1 epochs from the original unprotected model. ▷ Eq. (17)
- 8 Separately optimize two randomly initialized models for E_2 epochs to obtain the fake experts. ▷ Eq. (18) (19)
- 9 Construct the MoE model. ▷ Eq. (20)
- 10 **# Model Obfuscation**
- 11 Distill the MoE teacher model for E_3 epochs to generate the protected student model $f_{\theta_j^p}(\cdot)$. ▷ Eq. (21)
- 12 **return** $f_{\theta_j^p}(\cdot)$.

13 Distribute each model-key pair and the encoder (i.e., $\{f_{\theta_j^p}(\cdot), k_j\}$ and $\mathcal{E}(\cdot, \cdot)$) to the corresponding legal user.

We also align the neuron attention of $f_{\theta_j^p}(\cdot)$ and $\mathcal{M}_j(\cdot)$ on the selected layers by minimizing

$$\mathcal{L}_{at} = \mathbb{E}_{x \sim \mathcal{W}} \left[\sum_{l \in T_{sel}} \mathcal{L}_{AT} \left(f_{\theta_j^p}^l(x), \mathcal{M}_j^l(x) \right) \right]. \quad (25)$$

(3) To ensure that input samples from different domains also share low MI in the latent space in the student model, contrastive representation distillation (CRD) [41] loss is incorporated. Given a tuple of teacher and student representations $(f_T^l(x_a), f_S^l(x_b))$, where x_a and x_b are two random images sampled from \mathcal{W} . It is a *positive* pair if the two inputs are from the same domain (e.g., $x_a \sim \mathcal{A}_j$ and $x_b \sim \mathcal{A}_j$). Conversely, it is a *negative* pair if the two inputs are sourced from different domains (e.g., $x_a \sim \mathcal{A}_j$ and $x_b \sim \mathcal{B}$). Let $q(f_T^l, f_S^l | d=1)$ and $q(f_T^l, f_S^l | d=0)$ denote the joint distributions for *positive* and *negative* pairs, respectively. The CRD loss is given by:

$$\begin{aligned} \mathcal{L}_{crd} = & - \sum_{l \in T_{sel}} \mathbb{E}_{q(f_T^l, f_S^l | d=1)} \left[\log \left(h^l(f_T^l, f_S^l) \right) \right] \\ & - N_{neg} \sum_{l \in T_{sel}} \mathbb{E}_{q(f_T^l, f_S^l | d=0)} \left[\log \left(1 - h^l(f_T^l, f_S^l) \right) \right], \end{aligned} \quad (26)$$

where $h^l(\cdot, \cdot)$ denotes a critic to determine if the two representations are positively paired, and whose parameters can be optimized in parallel with \mathcal{L}_{crd} . We provide one *positive* pair for every N_{neg} *negative* pairs during training, with the aim to pull the *positive* pairs closer and push the *negative* pairs apart.

The protected model $f_{\theta_j^p}(\cdot)$ has similar performance as the MoE model $\mathcal{M}_j(\cdot)$, but the functionalities and hidden-layer behaviors of the three experts have been indistinguishably blended into a coherent network, making it infeasible for the adversary to extract the real expert model. The algorithm for generating the M encoded models $\{f_{\theta_j^p}(\cdot), k_j\}_{j=1}^M$ is depicted in Algorithm 1.

TABLE I: Specifications of the experimental datasets.

Dataset	# Labels	Input Size	# Training / Test Images
CIFAR-10	10	32×32	50000 / 10000
CIFAR-100	100	32×32	50000 / 10000
GTSRB	43	32×32	39208 / 12630
Caltech-101	101	32×32	6942 / 1735
ImageNet-10	10	224×224	12000 / 1000

D. Ownership Verification and Culprit Tracing

Intercepted image decoding. An adversary can be tracked by extracting the key from queries submitted to the suspected model by using the SteganoGAN decoder, which is kept private by the model owner. If the calculated Hamming distance (HD) between the key \hat{s} extracted from the intercepted test image and each user key recorded by the model owner exceeds a predetermined threshold, the user of that recorded key is identified as the culprit.

Given a set of intercepted images D_{int} and a threshold ϵ_3 , we define the tracing success rate (TSR) as

$$\text{TSR}(k, D_{int}) = \mathbb{E}_{x \sim D_{int}} [\mathbb{I}[\text{HD}(k, \text{Vote}(\text{Split}(\mathcal{D}(x)))) \leq \epsilon_3]], \quad (27)$$

where k denotes a recorded user key. $\mathbb{I}[\cdot, \cdot]$ is another indicator function which returns 1 if the HD between the recorded and decoded keys does not exceed ϵ_3 , and 0 otherwise.

Unfortunately, this tracing method requires the owner to intercept key-embedded input samples before the inference stage, which can be difficult sometimes. Moreover, the ownership of the suspected model cannot be attested.

Black-box query. The owner can also extract the user key from a black-box suspected model by performing a series of queries and analyzing the outputs. Specifically, an innocent model learns nothing about the user key will maintain the same high accuracy on both benign and key-embedded test samples. A pirated or redistributed model performs well only on authorized images encoded with a valid key. The dishonest user can be identified by the correct key that unlocks the original performance of the misappropriated model.

V. EXPERIMENTS

A. Experimental Setting

1) *Datasets and Networks:* Table I specifies the five public image classification datasets, CIFAR-10 [42], CIFAR-100 [42], GTSRB [43], Caltech-101 [44], and ImageNet [45], with different resolutions and numbers of classes. To speed up the training without loss of generality, we perform the ImageNet evaluation on its subset of 10 arbitrarily selected classes named ImageNet-10. The real and fake experts share the same architecture across ResNet-18 (Res-18) [46], PreActResNet-18 (PreRes-18) [46], SENet [47] and MobileNet-V2 (Mob-V2) [48].

2) *Key size:* We set r according to the input size of the dataset. For ImageNet-10, r is set to 32, which gives a key space of $2^{32 \times 32}$. The 32×32 key is replicated 49 times and then squarely concatenated to the same size of 224×224 as the benign images before they are input to the SteganoGAN encoder. For the other four datasets, we set r to 16 with a key

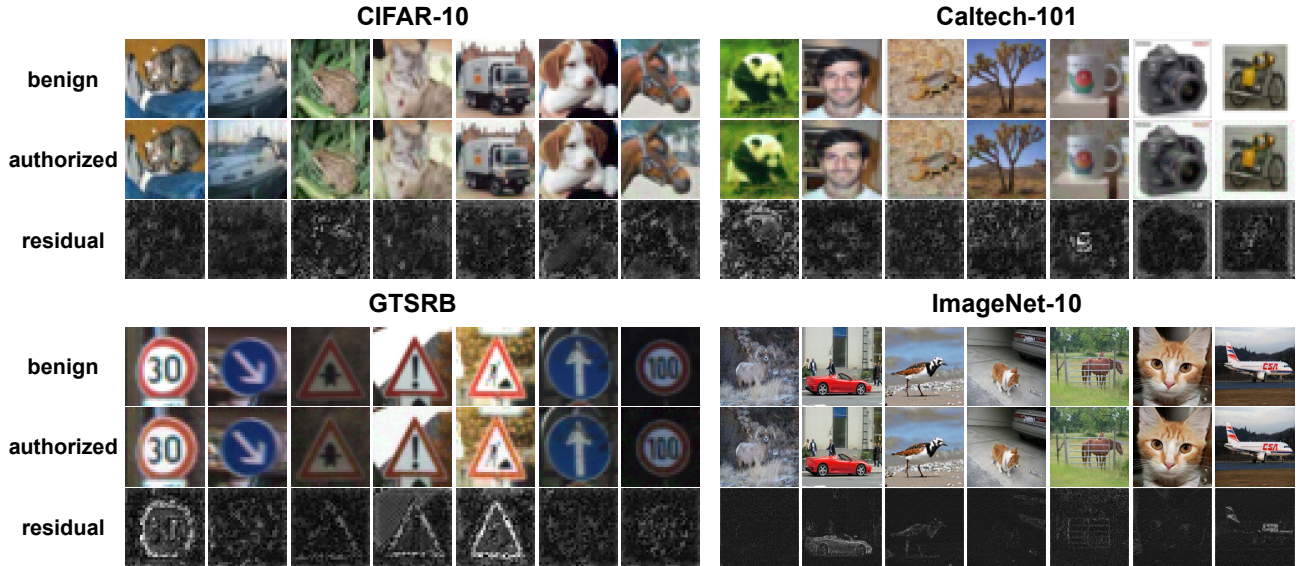


Fig. 4: Examples of benign (first row) and authorized (second row) images. For each dataset, all authorized images are embedded with the same binary key, and the magnified ($\times 10$) residual images are shown in the third row.

TABLE II: IQA scores of authorized images. \uparrow denotes larger value is better, and \downarrow denotes smaller value is better.

Dataset	IQA Metric		
	SSIM (\uparrow)	PSNR (\uparrow)	LPIPS (\downarrow)
CIFAR-10	0.9928 ± 0.0050	33.1038 ± 1.5923	0.0032 ± 0.0025
CIFAR-100	0.9908 ± 0.0081	32.6107 ± 2.0546	0.0033 ± 0.0027
GTSRB	0.9914 ± 0.0129	32.4346 ± 2.1956	0.0032 ± 0.0028
Caltech-101	0.9882 ± 0.0082	33.9264 ± 2.2390	0.0053 ± 0.0030
ImageNet-10	0.9706 ± 0.0249	35.3929 ± 1.4052	0.0144 ± 0.0089

space of $2^{16 \times 16}$. The 16×16 key is replicated four times and concatenated to the size of 32×32 .

3) *Other settings*: For each classification task, a dedicated SteganoGAN model is trained using 2500 samples randomly selected from the benign training dataset. The unprotected model $f_{\theta}(\cdot)$ is trained from scratch for 200 epochs, and from which the real expert $f_{\theta^R}(\cdot)$ is fine-tuned for 40 epochs, both using the Stochastic Gradient Descent optimizer. Each fake expert is separately trained for 1000 iterations. During the knowledge distillation process, the student model is optimized from scratch for 50 epochs using the Adam optimizer. Ten protected models are generated from the same source model with different random keys for distribution to ten different users. Several common data augmentations, including random cropping, random horizontal flipping, random rotation and random erasing, are applied during training to alleviate overfitting.

B. Evaluation

1) *Stealthiness*: Fig. 4 presents some examples of benign and authorized images for CIFAR-10, Caltech-101, GTSRB, and ImageNet-10 datasets. We also provide the magnified ($\times 10$) residual images obtained by the absolute difference in pixel values between the benign and authorized images. The perturbations introduced by SteganoGAN encoding are visually imperceptible. In other words, the attacker can hardly figure out the embedded key by inspecting a few test images encoded with the same key. Furthermore, the perturbations are

sample-specific. Even if the attacker can compute a residual image from a pair of benign and authorized image of a protected model, it is impossible to generate an authorized image by adding the residual image to a different test image. The means and standard deviations of three objective image quality assessments (IQA), Structural Similarity Index Measure (SSIM) [49], Peak Signal to Noise Ratio (PSNR) and Learned Perceptual Image Patch Similarity (LPIPS) [50] are presented in Table II. The outstanding IQA scores prove the stealthiness of the key-encoded images.

2) *Effectiveness and fidelity*: The inference performances of both unprotected and protected models on benign, authorized, and noise test images are presented in Table III. The results indicate that unprotected models consistently achieve high prediction accuracy across all three domains. All protected models fulfill the **fidelity** requirement of Eq. (4), with inference accuracy of authorized images comparable to the benign accuracy of the corresponding unprotected model. The accuracy drop is no more than 1.5%. Additionally, the protected models perform poorly on benign and noise images, with near-random guessing accuracies, making them useless to unauthorized users without the correct key.

3) *Uniqueness*: We trained 10 protected models encoded with different keys and evaluated the prediction performance across all possible combinations of model-key pairs. The confusion matrices are presented in the first row of Fig. 5, where each row denotes a protected model and each column denotes a key. The diagonal and off-diagonal values represent test accuracies for matched and mismatched model-key pairs, respectively. All but the diagonal values of these confusion matrices are very low ($< 20\%$), indicating that user keys among protected models are non-exchangeable. Therefore, the protected model of one legitimate user cannot achieve accurate prediction on encoded images generated with another legitimate user's key.

An attacker may have stolen a protected model and the

TABLE III: Prediction accuracy (%) of unprotected and protected models on benign/authorized/noise test images across different networks and datasets. For each case, the unprotected model’s performance on benign dataset is highlighted in **blue** and set as the baseline; the protected model’s performance on authorized dataset is highlighted in **green**. The acc. change (%) is calculated by subtracting the former from the latter.

Dataset	Model	Test on benign / authorized / noise images(%)			
		Res-18	PreRes-18	SENet	Mob-V2
CIFAR-10	unprotected	93.58 / 91.87 / 91.99	93.82 / 91.83 / 92.08	93.68 / 92.07 / 92.15	91.63 / 89.66 / 89.84
	protected	10.13 / 93.15 / 9.69	12.66 / 93.00 / 14.70	1.79 / 93.10 / 12.18	10.06 / 91.37 / 12.72
	acc. change (%)	-0.43	-0.82	-0.58	-0.26
CIFAR-100	unprotected	73.31 / 69.09 / 68.72	73.69 / 67.52 / 67.26	73.48 / 68.15 / 68.29	69.82 / 65.06 / 64.68
	protected	1.33 / 73.10 / 1.40	1.19 / 72.91 / 1.50	1.37 / 72.93 / 1.91	1.03 / 71.36 / 2.25
	acc. change (%)	-0.21	-0.78	-0.55	1.54
Caltech-101	unprotected	75.73 / 75.73 / 76.02	76.71 / 76.60 / 76.37	76.08 / 75.68 / 75.79	75.91 / 75.22 / 75.79
	protected	1.04 / 77.23 / 1.38	1.56 / 77.81 / 1.27	0.40 / 75.62 / 1.10	1.90 / 76.02 / 2.59
	acc. change (%)	1.50	1.10	-0.46	0.11
GTSRB	unprotected	97.29 / 92.26 / 92.98	98.01 / 92.77 / 92.89	97.11 / 91.94 / 93.86	98.74 / 97.24 / 97.14
	protected	2.01 / 97.78 / 3.33	5.34 / 97.95 / 5.57	1.15 / 97.75 / 2.68	6.94 / 98.12 / 5.84
	acc. change (%)	0.49	-0.06	0.64	-0.62
ImageNet-10	unprotected	88.85 / 88.69 / 88.81	89.38 / 89.23 / 89.38	88.81 / 88.58 / 88.77	85.92 / 86.27 / 85.96
	protected	10.35 / 89.31 / 10.08	10.46 / 87.88 / 11.96	9.88 / 89.42 / 9.04	10.31 / 87.69 / 11.31
	acc. change (%)	0.46	-1.50	0.61	1.77

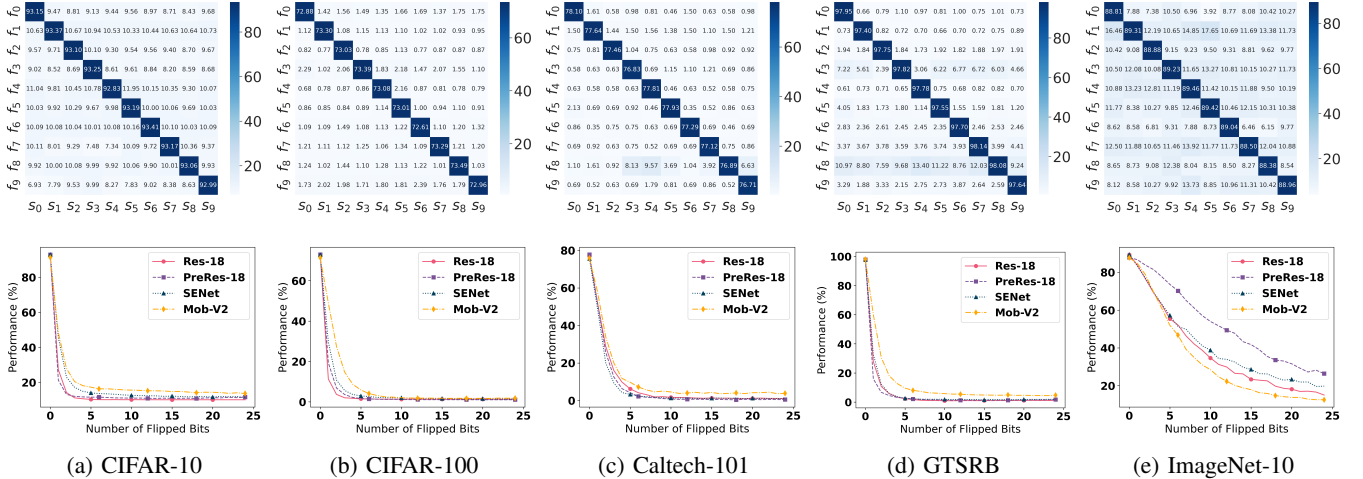


Fig. 5: Uniqueness evaluation of IDEA. Row 1: confusion matrices for the evaluation of 10 different keys on the 10 encoded models. ResNet-18 is the architecture used for all the protected models. Row 2: Accuracies of the protected models on test images embedded with incorrect keys with a few erroneous bits.

SteganoGAN encoder from a legitimate user. Without the legitimate user key, the complexity of brute force key guessing is $O(2^r)$, provided that the protected model produces random output to any input images generated by the stolen encoder with the wrong guessed key even if the guessed key contains only one error bit. To evaluate the tolerance of the protected model to bit errors in the key used for encoding the test images, we randomly flipped a few bits, ranging from 1 to 24, of the user keys. As shown in the second row of Fig. 5, for the four low-resolution datasets, all protected models suffer from severe performance degradation with just one error bit. Although the accuracies do not drop to the level of random prediction, they are unacceptably low. When the number of flipped bits has increased to 3, the prediction accuracies of all protected models have dropped to no more than 21%. On the other hand, for ImageNet-10, the accuracies of the models degraded slower with the number of flipped bits. The

accuracies dropped by only around 4% with just one bit flip in the user key. However, all four models experienced a performance degradation of more than 40% when 13 key bits are flipped. Considering the image resolution (1024 bits), it is still computationally intractable to successfully brute force 13 correct key bits.

4) *Verification and tracing performance*: For each dataset, we select 1,000 benign test images and encode them with 10 different keys, k_1, k_2, \dots, k_{10} , to simulate an intercepted dataset D_{int} that contains 10000 images embedded with unknown keys. These images are fed into the private SteganoGAN decoder to extract their embedded keys. We set the threshold ϵ_3 of Eq. (27) to 1, which is the most stringent threshold with at most one bit difference allowed. Table IV demonstrates that an extremely high TSR of over 97% is achievable across all datasets and keys, with an average TSR of above 99% for all five datasets. With such a high TSR, the owner can easily pinpoint the culprit with high confidence,

TABLE IV: TSRs (%) obtained by comparing correct keys and decoded keys from intercepted images with the private SteganoGAN decoder.

Dataset	Key										Avg. TSR
	k_1	k_2	k_3	k_4	k_5	k_6	k_7	k_8	k_9	k_{10}	
CIFAR-10	99.0	100.0	100.0	100.0	100.0	99.9	99.7	100.0	99.9	100.0	99.85
CIFAR-100	97.4	99.5	99.4	99.8	99.7	99.3	99.7	99.6	99.7	99.3	99.34
Caltech-101	97.9	99.2	99.3	99.1	99.0	98.8	98.8	99.4	99.4	99.3	99.02
GTSRB	99.7	99.8	100.0	100.0	100.0	99.8	100.0	100.0	99.9	99.7	99.89
ImageNet-10	100.0	100.0	100.0	100.0	100.0	100.0	99.9	100.0	100.0	100.0	99.99

TABLE V: Tracing accuracy (%) of the black-box query on 20 suspected models. A suspected model is successfully traced if: 1) it is actually a benign model and identified as innocent; 2) it is correctly identified as a pirated model, and the dishonest buyer is correctly traced.

Network	Dataset				
	CIFAR-10	CIFAR-100	Caltech-101	GTSRB	ImageNet-10
Res-18	100	100	100	100	100
PreRes-18	100	100	100	100	100
SENet	100	100	100	100	100
Mob-V2	100	100	100	100	100

even if only one encoded image is accessible.

To evaluate the verification and tracing performance of black-box query, we create a query dataset D_q of 100 benign test images and encode them with 10 different keys to produce 10 encoded query datasets, $D_q^0, D_q^1, \dots, D_q^9$. We also train 10 benign models from scratch using the benign training dataset and mix them with the 10 protected models to create a suspected model set of 10 innocent models and 10 protected models pirated from different users. It is observed that innocent models consistently achieve high performance on all query datasets, regardless of the embedded keys. In contrast, pirated models perform optimally (with 70% to 90% accuracy depending on the dataset) only on a single query dataset embedded with the correct key, and poorly (with < 20% accuracy) otherwise. The tracing accuracy (TA) of black-box query can be computed as:

$$TA = \frac{\text{number of successfully traced models}}{\text{number of suspected models}} \times 100\%, \quad (28)$$

Table V shows that 100% TA is achieved across all datasets and networks, which confirms the excellent ownership verification and culprit tracing accuracy of IDEA.

C. Active Protection Methods Comparison

We re-implemented four recent active protection methods, DeepIPR [19], SSAT [21], DSN [24], and pixel shuffling [18], on ResNet-18 across the five datasets for comparison. We also directly distilled a student model from the MoE model with only KL-divergence and *without* attention and contrastive representation loss terms. We call this model the “simple-distilled model”. Table VI presents the accuracies of the protected models on authorized and benign test images. The accuracy change for each protected model and dataset is also provided in bracket.

The performance of the pixel shuffling [18] method is dependent on the shuffling block size b , which trades model’s accuracy on unauthorized images for model’s accuracy on authorized images. For low-resolution datasets, $b = 2$ provides a good trade-off between effectiveness and fidelity. For ImageNet-10, it can only keep the prediction accuracy of the unauthorized images to below 50% by degrading the accuracy of authorized images by more than 5% with optimal $b = 8$.

DeepIPR [19], SSAT [21], and DSN [24] can keep the accuracy drop to lower than 1.5% on authorized images and sufficiently degrade the performance on unauthorized images (<40%). However, these three methods have their own security vulnerability. The passport layers of DeepIPR can be easily localized since they require additional inputs. The attacker can replace these passport layers with custom normalization layers and re-train them to achieve high accuracy on benign images without passport inputs, as demonstrated in [51]. SSAT assigns ground truth labels to poisoned training samples and wrong labels to clean training samples. The ground-truth label y of clean input image is mapped to the wrong label $y' = y + 1$. This fixed bijective mapping can be easily reverse-engineered by observing the model’s outputs to a small set of labeled test images. Any other deterministic bijective mapping is as vulnerable. The DSN method directly pastes a fixed binary pattern on the test images as secret key, which can be easily spotted by human eyes.

IDEA achieves good effectiveness and fidelity on all datasets. Layer substitution attack is not able to break IDEA as we make no modification to the model architecture. Query-based reverse-engineering is also infeasible as the outputs of unauthorized images are randomized. Since the perturbations introduced by SteganoGAN encoder are imperceptible and sample-specific, it is impossible for the attacker to recognize and copy the secret key.

Although the simple-distilled model can achieve similar classification accuracy as the protected model, their differences will be more closely scrutinized in Sec. VI.

VI. A CLOSER LOOK AT LATENT REPRESENTATIONS

In this section, the hidden layer outputs of the unprotected, MoE, simple-distilled and protected models are examined from three perspectives: MI estimation, attention map visualization, and representation visualization.

A. MI Estimation

Fig. 6 visualizes the estimated MI between the latent representations collected from paired source (authorized) and target (unauthorized) test samples, with the first row showing the MI between authorized and benign images, and the second row showing the MI between authorized and noise images. Layers 1 to 4 are the selected layers for MI minimization and multi-layer attention and contrastive representation knowledge distillation, progressing from the shallow to deep layer.

For all selected layers, we observe that the estimated MI on the unprotected model is consistently high. This is expected, as this model has not been trained to recognize steganographic

TABLE VI: Comparison with existing active DNN IP protection methods on prediction performance (%) on authorized and benign test datasets. $y' = y + 1$ is the wrong label of a clean image with ground truth label y . b is the block size of the pixel-shuffling key. Ours \ddagger denotes the simple-distilled model that is trained with only the KL-divergence loss.

Method	Dataset \rightarrow	CIFAR-10		CIFAR-100		Caltech-101		GTSRB		ImageNet-10	
	Setting \downarrow	authorized	benign	authorized	benign	authorized	benign	authorized	benign	authorized	benign
DeepIPR [19]	-	93.07 (-0.51)	7.82	72.08 (-1.23)	2.56	74.89 (-0.84)	4.30	97.55 (+0.26)	11.75	87.82 (-1.03)	28.51
SSAT [21]	$y' = y + 1$	93.53 (-0.05)	0.60	72.95 (-0.36)	0.21	76.04 (+0.31)	0.81	97.85 (+0.56)	0.41	87.57 (-1.28)	2.10
DSN [24]	-	93.06 (-0.52)	11.55	72.42 (-0.89)	2.22	77.11 (+1.38)	1.10	97.97 (+0.68)	1.51	89.04 (+0.19)	10.96
Pixel Shuffling [18]	$b = 2$	92.41 (-1.17)	44.71	67.53 (-5.78)	10.87	73.48 (-2.25)	41.27	96.61 (-0.68)	8.52	86.89 (-1.96)	58.45
	$b = 4$	89.28 (-4.30)	23.78	57.48 (-15.83)	3.45	64.84 (-10.89)	17.46	94.46 (-2.83)	8.80	84.93 (-3.92)	56.50
	$b = 8$	82.36 (-11.22)	20.07	42.27 (-31.04)	5.33	53.14 (-22.59)	5.24	88.19 (-9.10)	5.09	83.37 (-5.48)	48.93
Ours \ddagger	\mathcal{L}_{kl}	92.84 (-0.74)	9.90	72.35 (-0.96)	1.90	77.35 (+1.62)	5.13	98.23 (+0.94)	1.64	89.88 (+1.03)	7.42
Ours	$\mathcal{L}_{kl}, \mathcal{L}_{at}, \mathcal{L}_{crd}$	93.15 (-0.43)	10.13	73.10 (-0.21)	1.33	77.23 (+1.50)	1.04	97.78 (+0.49)	2.01	89.31 (+0.46)	10.35

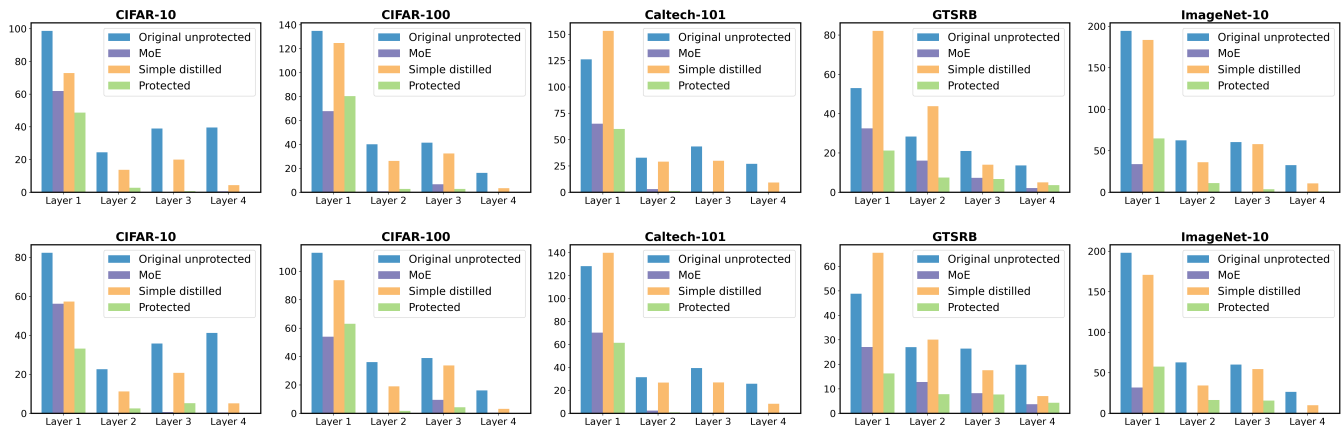


Fig. 6: Estimated MI between the latent features of test images in the source (authorized) and target (unauthorized) domains. Due to the resolution of the vertical scale, some bars are not visible because their estimated MI values are very close to 0. Row 1: MI between paired authorized and benign images. Row 2: MI between paired authorized and noise images.

perturbations and thus produces similar representations for all types of images. In contrast, the MI between the source and target images estimated on the MoE model is significantly lower than that on the unprotected model, demonstrating that the training objectives in Eqs. (18) and (19) effectively increase the expected risk of the two fake experts. The protected model also shows similarly low MI values, indicating that the protected model faithfully emulates the MoE model’s behavior across all selected layers. Consequently, if the input images are not embedded with the correct key, the adversary can only obtain meaningless intermediate layer representations that are comparable to those output by the fake experts. However, the MI estimated on the simple-distilled model is higher than that of the MoE and protected models, and in some cases even higher than that of the unprotected model. This indicates that using only KL-divergence constraints on the output layer during knowledge distillation is insufficient to protect the model functionalities. Specifically, the shallow layers of the simple-distilled model exhibit good generalizability on the target domains, making it easier to break the active authorization protection through fine-tuning, as these well-performing shallow layers require almost no adjustment.

B. Attention Map Visualization

Fig. 7 shows the attention maps generated at the output of selected layers by feeding paired benign/authorized/noise test images into the four models. It shows that the unprotected model outputs similar attention maps for all three domains of

test images at all selected layers. Conversely, the MoE model produces similar attention maps to the unprotected model only on input of authorized images. On input of benign or noise images, the MoE model exhibits attention behaviors akin to an untrained model to these inputs. Moreover, the protected model perfectly imitates the intermediate layer behaviors of the MoE model, as it outputs almost identical attention maps as those of the MoE model for the same domains of test images at all the selected layers. However, the simple-distilled model exhibits similar attention maps for all types of images at the first three selected layers, and these attention maps are similar to those of the unprotected model at the same layers.

C. t-SNE Visualization of Latent Representation

We randomly selected 500 benign images from the ImageNet-10 dataset and generated their authorized and noise versions to create a mixed test set with 1500 images. These test images were separately fed into the four models, and their outputs at the four selected layers were collected. The latent representations of the three types of test images are visualized using the t-SNE [38] in Fig. 8. For the unprotected model, the points corresponding to the paired benign/authorized/noise images almost completely overlap across all selected layers. This further illustrates that the source and target images have high estimated MI at the hidden layers. The simple-distilled model has similar behaviors in layers 1 to 3, but the representations in layer 4 form three distinct clusters. This result, again, reveals that the simple-distilled model has good

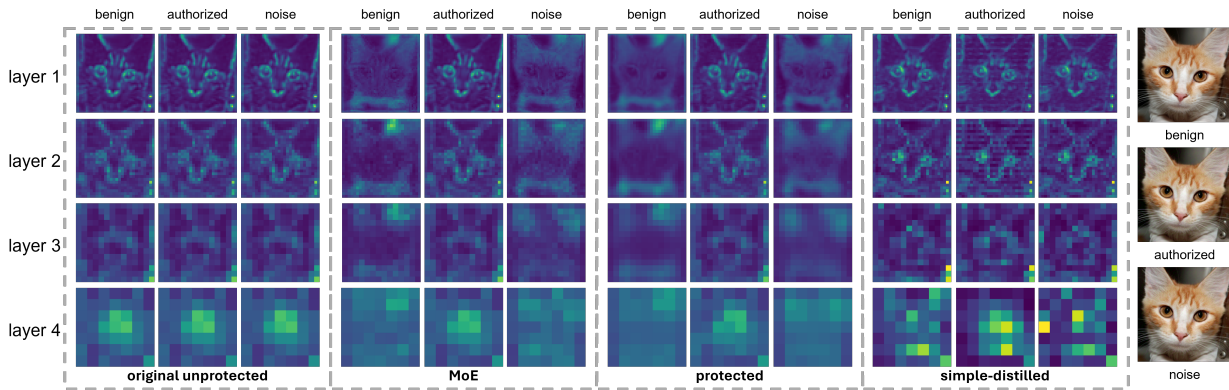


Fig. 7: Visualization of attention maps generated by the original unprotected, MoE, protected and simple-distilled models, respectively. The test images are randomly selected from ImageNet-10.

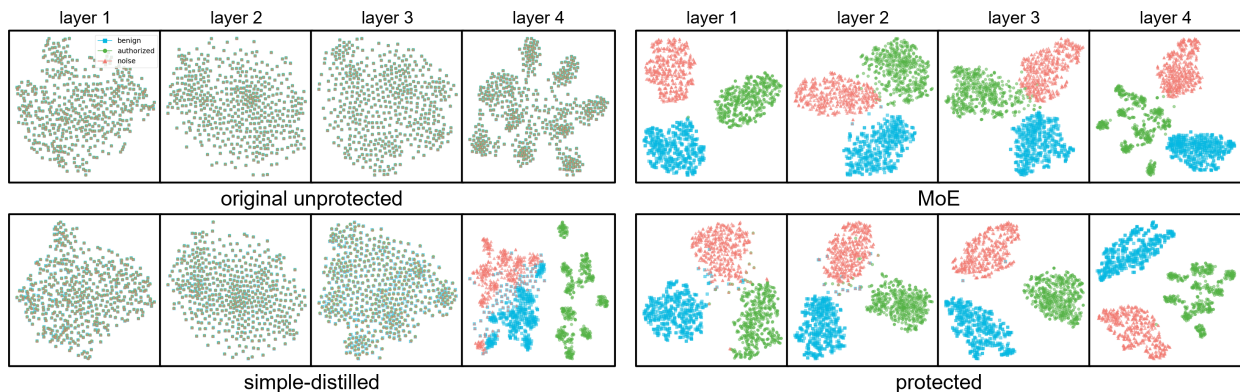


Fig. 8: t-SNE visualization of the latent representations of the original unprotected (top left), simple-distilled (bottom left), MoE (top right) and protected (bottom right) models obtained from 1500 ImageNet-10 test images. The latent representations of the benign/authorized/noise test images are shown as blue squares, green dots, and red triangles, respectively.

generalizability at the shallow layers, and the representations of the three types of images are indistinguishable until the deep layers. On the contrary, for the MoE and protected models, the points corresponding to benign/authorized/noise images are well clustered across all selected layers. This indicates that the MI minimization has successfully made the two fake experts behave differently from the real expert, and the protected model effectively mimics the behavior of the MoE model at not only the output layer but also the selected hidden layers.

VII. SECURITY ANALYSIS

We further investigate the robustness of IDEA against both model transformation and reverse-engineering attacks. Model transformation attacks aim to remove the active authorization protection by directly modifying the pirated model through fine-tuning, model-pruning, and transfer-learning. Reverse-engineering attacks aim to reverse engineer the encoding process without modifying the pirated model.

Model Transformation Attacks

Fine-tuning. Following the configurations in [52], we apply the following four fine-tuning strategies, fine-tune all layers (FTAL), fine-tune last layer (FTLL), re-train all layers (RTAL), and retrain last layer (RALL) on the protected model.

- FTAL: The weights in all the layers are updated.
- FTLL: Only the weights in the last layer are updated.

- RTAL: The weights in the last layer are randomly initialized, and then the weights in all the layers are updated.
- RTLL: The weights in the last layer are randomly initialized, but only the weights in the last layer are updated.

The protected model is fine-tuned for 30 epochs using 10%, 20%, and 30% of the samples from the benign training dataset. For comparison, we also conduct the same attacks on the simple-distilled model.

Table VII shows the accuracy of the fine-tuned models on the benign test dataset. The baseline performance of the unprotected models on the benign test dataset is shown in the last column. For fine-tuned protected models, the performance improves with increasing ratio of accessible samples. However, even with 30% training samples, the inference accuracy on benign data is still significantly lower than the baseline performance. In most cases, the model fine-tuned from the simple-distilled model has higher accuracy than from the protected model, especially for FTAL. This result agrees with our observation in Sec. VI that the shallow layers of the simple-distilled model can be exploited for fine-tuning attack. Therefore, the multi-layer attention and contrastive representation losses are required to prevent the distilled shallow layers from leaking the real expert functionality of the teacher model.

Model-pruning. Weight pruning (WP) and filter pruning (FP), are commonly used to reduce model size by remov-

TABLE VII: Accuracy (%) of fine-tuned models on benign test datasets. The last column lists the baseline classification accuracy of the unprotected models on benign test datasets.

Dataset	Ratio	Protected model				Simple-distilled model				baseline
		FTAL	FLL	RTAL	RTL	FTAL	FLL	RTAL	RTL	
CIFAR-10	10 %	58.38	57.00	60.58	58.46	82.27	83.62	87.26	69.51	93.58
	20 %	60.82	58.98	62.01	65.74	88.52	85.47	91.60	73.58	
	30 %	61.54	58.73	64.86	66.18	90.23	86.33	92.28	75.92	
CIFAR-100	10 %	45.73	41.91	26.46	22.39	58.36	41.92	22.32	20.28	93.31
	20 %	47.12	41.54	40.83	32.51	66.02	41.59	41.67	32.00	
	30 %	49.00	42.46	50.12	39.47	68.08	41.69	47.38	36.53	
Caltech-101	10 %	53.95	52.80	38.16	32.91	60.00	51.47	33.72	31.99	75.73
	20 %	55.27	52.05	48.47	39.31	62.88	53.31	39.02	35.62	
	30 %	56.48	52.80	57.69	42.54	63.63	55.62	48.36	40.35	
GTSRB	10 %	50.78	47.28	11.08	9.33	68.31	53.82	12.10	9.64	97.29
	20 %	54.13	46.17	20.51	14.49	89.52	54.08	20.85	16.20	
	30 %	56.37	41.52	29.95	20.07	92.62	48.51	30.48	22.22	
ImageNet-10	10 %	64.35	70.19	60.77	62.69	78.27	80.08	85.38	78.08	88.85
	20 %	72.77	70.46	70.81	71.00	81.65	81.88	88.00	79.31	
	30 %	72.35	70.54	69.88	73.04	83.00	83.04	88.96	80.12	

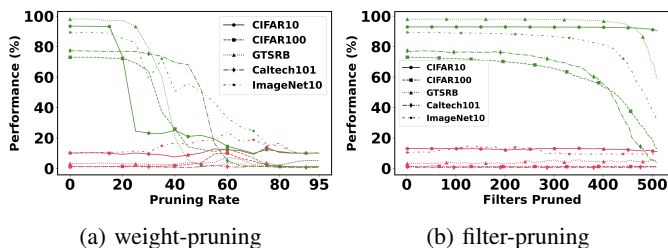


Fig. 9: Robustness of IDEA against weight-pruning and filter-pruning attacks. We present the pruned models’ performance on authorized and benign (unauthorized) test datasets in green and red, respectively.

ing parameters that contribute insignificantly to inference performance [53]. WP globally prunes a fraction (ranging from 5% to 95%, with a step size of 5%) of the smallest magnitude weights. FP iteratively prunes filters in a specific convolutional layer, starting from the smallest magnitude to the largest. Following the configuration in [54], we select the last convolutional layer of ResNet-18 as the target layer for FP implementation.

The results are shown in Fig. 9. For WP, the accuracy of the protected model on both test images with and without the correct user key embedded changes minimally when the pruning rate is less than 30%. As the pruning rate increases, the inference performance of test images embedded with correct user key drops sharply due to the removal of some crucial weights. Nevertheless, the accuracy on benign test images remains consistently low across all pruning rates. Similarly, the accuracy on benign test images falls below 20% consistently across all datasets regardless of the number of filters pruned by the FP attack. As the functionalities of real and fake experts are tightly coupled by knowledge distillation, it is infeasible to disable the active authorization by merely pruning weights or filters without sacrificing the inference accuracy.

Transfer-learning. This attack aims to utilize the well-trained feature extractor to adapt the pirated model to a different task using a private dataset. The common transfer-learning paradigm freezes all layers except the last fully connected layer, which is randomly initialized based on the

new task. For the four low-resolution datasets, we perform transfer learning on both unprotected and protected models using other low-resolution datasets. For the high-resolution ImageNet-10, we select another 10 classes from the entire ImageNet dataset to form a non-overlapping subset ImageNet-10† for transfer-learning. The results in Tabel VIII show that models that are transfer-learnt from protected models exhibit worse performance than from unprotected models as protected models output meaningless features by imitating fake experts.

Reverse-engineering Attacks

This kind of attacks assumes that the adversary has successfully stolen a protected model from a legitimate user, but not the SteganoGAN encoder and the correct user key. We make two assumptions about the data available to the attacker.

Assumption 1: The attacker only has a small portion of the benign images to train a generator $\mathcal{G}(\cdot)$ to produce encoded images for the pirated model. The optimization objective of the generator can be expressed as follows:

$$\arg \min \mathbb{E}_{(x,y) \sim \mathcal{D}_{\text{sub}}} \left[\mathcal{L}_{\text{CE}}(f_{\theta_j^p}(\mathcal{G}(x)), y) \right], \quad (29)$$

where \mathcal{D}_{sub} denotes the benign subset hold by the attacker.

Assumption 2: The attacker has not only a small portion of benign images but also their authorized versions embedded with the correct key by eavesdropping on legitimate users. This scenario enables the attacker to train the generator more efficiently by simultaneously minimizing the MSE loss between the generated and authorized images as follows:

$$\arg \min \mathbb{E}_{(x,y) \sim \mathcal{D}_{\text{sub}}} \left[\mathcal{L}_{\text{CE}}(f_{\theta_j^p}(\mathcal{G}(x)), y) + \lambda_4 \mathcal{L}_{\text{MSE}}(\mathcal{G}(x), x_j^+) \right], \quad (30)$$

where λ_4 is a weighting factor.

We simulate these attacks by training a generator with different numbers of benign images or benign-authorized pairs, ranging from 500 to 5000. The generator has a similar architecture to the SteganoGAN encoder but without the key input port. Both its input and output are 3-channel color images of the same size. Table IX reports the accuracy of the pirated model on test images created by the generator. Under *Assumption 1*, most reverse-engineering attacks result in low prediction accuracy close to random guessing. The best attack performance achieved on Caltech-101 with 5000 available benign images is merely 22.13%. As expected, the

TABLE VIII: Accuracy (%) of models trained using transfer-learning from unprotected and protected models. The original training datasets are listed in the first row and the private dataset to be adapted in the first column. ImageNet-10[†] is another subset of ImageNet consisting of 10 classes that do not overlap with ImageNet-10.

Dataset	CIFAR-10		CIFAR-100		Caltech-101		GTSRB		ImageNet-10 [†]	
	unprotected	protected	unprotected	protected	unprotected	protected	unprotected	protected	unprotected	protected
CIFAR-10	-	-	30.41	17.39	37.35	26.05	50.85	22.80	-	-
CIFAR-100	75.25	61.47	-	-	55.50	30.14	65.69	36.66	-	-
Caltech-101	68.17	54.62	41.73	26.13	-	-	63.06	43.95	-	-
GTSRB	46.78	35.43	18.70	10.17	31.99	20.00	-	-	-	-
ImageNet-10	-	-	-	-	-	-	-	-	50.34	40.36

TABLE IX: Accuracy (%) of pirated models on reverse-engineered images generated based on Assumptions 1 and 2.

Dataset	Assumption	# Available images / pairs				
		500	1000	2000	3000	5000
CIFAR-10	1	9.67	12.23	12.12	10.06	10.00
	2	10.00	12.71	13.39	16.06	56.84
CIFAR-100	1	1.08	0.91	1.00	1.00	1.01
	2	1.11	1.26	1.74	1.76	10.24
Caltech-101	1	0.98	1.21	8.47	1.21	22.13
	2	1.04	5.53	22.71	29.80	37.46
GTSRB	1	4.99	4.96	5.70	4.99	0.56
	2	4.05	3.52	30.11	34.70	44.51
ImageNet-10	1	9.65	10.19	16.15	14.38	15.92
	2	10.23	10.92	15.58	16.19	27.85

attack performance under *Assumption 2* is much better in most cases, with an average improvement of 9.55%. However, even with 5000 available benign-authorized pairs, which are difficult for the attacker to collect in reality, the best attack performance of 56.84% achievable on CIFAR-10 is still far lower than the baseline. Therefore, IDEA is resilient against even the strongest assumption of reverse-engineering attacks.

VIII. CONCLUSION

We have presented a novel active DNN IP protection method called IDEA. It steganographically encodes distributed model instances with user-specific keys. The authorized user of a protected model instance can unlock its inference performance by submitting test images embedded with a valid key assigned by the model owner. In the event of IP infringement, the owner can verify the authenticity of deployed models and trace the culprit by querying the suspected model with a small set of test samples or decoding the user submitted queries. Extensive experiments conducted across five image classification datasets and four DNN models validated the excellent inference performance on authorized inputs, and corroborated that IDEA-protected models cannot be unlocked by images encoded with incorrect keys even with only a few flipped bits or keys stolen from other legitimate users. This strong uniqueness property is important to assure that the tracking of any redistributed purchased models to its culprit is non-repudiable. The culprit can be traced by decoding the intercepted test images with almost 100% success rate. IDEA is also robust against model transformation and reverse-engineering attacks, and more stealthy, effective, and scalable with networks and dataset sizes compared with existing active protection methods.

REFERENCES

[1] F. Tramèr *et al.*, “Stealing machine learning models via prediction apis,” in *Proc. USENIX Secur. Symp.*, 2016, pp. 601–618.

[2] T. Orekondy, B. Schiele, and M. Fritz, “Knockoff nets: Stealing functionality of black-box models,” in *Proc. IEEE/CVF Conf. Comput. Vis. Pattern Recognit.*, 2019, pp. 4954–4963.

[3] S. Kariyappa, A. Prakash, and M. K. Qureshi, “Maze: Data-free model stealing attack using zeroth-order gradient estimation,” in *Proc. IEEE/CVF Conf. Comput. Vis. Pattern Recognit.*, 2021, pp. 13814–13823.

[4] A. S. Rakin, M. H. I. Chowdhury, F. Yao, and D. Fan, “Deepsteal: Advanced model extractions leveraging efficient weight stealing in memories,” in *Proc. IEEE Symp. Secur. Privacy.* IEEE, 2022, pp. 1157–1174.

[5] S. Sanyal, S. Addepalli, and R. V. Babu, “Towards data-free model stealing in a hard label setting,” in *Proc. IEEE/CVF Conf. Comput. Vis. Pattern Recognit.*, 2022, pp. 15284–15293.

[6] Y. Uchida, Y. Nagai, S. Sakazawa, and S. Satoh, “Embedding watermarks into deep neural networks,” in *Proc. ACM Int. Conf. Multimedia Retrieval*, 2017, pp. 269–277.

[7] E. Le Merrer, P. Perez, and G. Trédan, “Adversarial frontier stitching for remote neural network watermarking,” *Neural Comput. Appl.*, vol. 32, pp. 9233–9244, 2020.

[8] Y. Adi *et al.*, “Turning your weakness into a strength: Watermarking deep neural networks by backdooring,” in *Proc. USENIX Secur. Symp.*, 2018, pp. 1615–1631.

[9] S. Szyller, B. G. Atli, S. Marchal, and N. Asokan, “Dawn: Dynamic adversarial watermarking of neural networks,” in *Proc. ACM Int. Conf. Multimedia*, 2021, pp. 4417–4425.

[10] H. Chen *et al.*, “Deepmarks: A secure fingerprinting framework for digital rights management of deep learning models,” in *Proc. ACM Int. Conf. Multimedia Retrieval*, 2019, pp. 105–113.

[11] T. Wang and F. Kerschbaum, “Riga: Covert and robust white-box watermarking of deep neural networks,” in *Proc. Web Conf.*, 2021, pp. 993–1004.

[12] R. Namba and J. Sakuma, “Robust watermarking of neural network with exponential weighting,” in *Proc. ACM Asia Conf. Comput. Commun. Secur.*, 2019, pp. 228–240.

[13] H. Jia *et al.*, “Proof-of-learning: Definitions and practice,” in *Proc. IEEE Symp. Secur. Privacy.* IEEE, 2021, pp. 1039–1056.

[14] X. Cao, J. Jia, and N. Z. Gong, “Ipguard: Protecting intellectual property of deep neural networks via fingerprinting the classification boundary,” in *Proc. ACM Asia Conf. Comput. Commun. Secur.*, 2021, pp. 14–25.

[15] Y. Li *et al.*, “Modeldiff: Testing-based dnn similarity comparison for model reuse detection,” in *Proc. ACM SIGSOFT Int. Symp. Softw. Testing Anal.*, 2021, pp. 139–151.

[16] Y. Zheng, S. Wang, and C.-H. Chang, “A dnn fingerprint for non-repudiable model ownership identification and piracy detection,” *IEEE Trans. Inform. Forensics Secur.*, vol. 17, pp. 2977–2989, 2022.

[17] A. Chakraborty, A. Mondai, and A. Srivastava, “Hardware-assisted intellectual property protection of deep learning models,” in *Proc. ACM/IEEE Des. Automat. Conf. IEEE*, 2020, pp. 1–6.

[18] A. Pyone, M. Maung, and H. Kiya, “Training dnn model with secret key for model protection,” in *Proc. IEEE Global Conf. Consum. Electronics.* IEEE, 2020, pp. 818–821.

[19] L. Fan, K. W. Ng, C. S. Chan, and Q. Yang, “Deepipr: Deep neural network ownership verification with passports,” *IEEE Trans. Pattern Anal. Mach. Intell.*, vol. 44, no. 10, pp. 6122–6139, 2021.

[20] N. Lin, X. Chen, H. Lu, and X. Li, “Chaotic weights: A novel approach to protect intellectual property of deep neural networks,” *IEEE Trans. Computer-Aided Des. Integr. Circuits Syst.*, vol. 40, no. 7, pp. 1327–1339, 2020.

[21] M. Xue *et al.*, “Ssat: Active authorization control and user’s fingerprint tracking framework for dnn ip protection,” *ACM Trans. Multimedia Comput. Commun. Appl.*, 2023.

- [22] J. Zhang *et al.*, “Protecting intellectual property of deep neural networks with watermarking,” in *Proceedings ACM Asia Conf. Comput. Commun. Secur.*, 2018, pp. 159–172.
- [23] G. Ren *et al.*, “Protecting intellectual property with reliable availability of learning models in ai-based cybersecurity services,” *IEEE Trans. Dependable Secure Comput.*, vol. 21, no. 2, pp. 600–617, 2022.
- [24] R. Tang, M. Du, and X. Hu, “Deep serial number: Computational watermarking for dnn intellectual property protection,” *arXiv preprint arXiv:2011.08960*, 2020.
- [25] Y. Ganin and V. Lempitsky, “Unsupervised domain adaptation by backpropagation,” in *Proc. Int. Conf. Mach. Learn.* PMLR, 2015, pp. 1180–1189.
- [26] L. Wang *et al.*, “Non-transferable learning: A new approach for model ownership verification and applicability authorization,” *arXiv preprint arXiv:2106.06916*, 2021.
- [27] J. Zhang *et al.*, “Passport-aware normalization for deep model protection,” *Proc. Adv. Neural Inform. Process. Syst.*, vol. 33, pp. 22 619–22 628, 2020.
- [28] H. Liu, Z. Weng, Y. Zhu, and Y. Mu, “Trapdoor normalization with irreversible ownership verification,” in *Proc. Int. Conf. Mach. Learn.* PMLR, 2023, pp. 22 177–22 187.
- [29] Q. Cui, R. Meng, C. Xu, and C.-H. Chang, “Steganographic passport: An owner and user verifiable credential for deep model ip protection without retraining,” in *Proc. IEEE/CVF Conf. Comput. Vis. Pattern Recognit.*, 2024, pp. 12 302–12 311.
- [30] B. Sun and K. Saenko, “Deep coral: Correlation alignment for deep domain adaptation,” in *Computer Vision—ECCV 2016 Workshops: Amsterdam, The Netherlands, October 8–10 and 15–16, 2016, Proceedings, Part III 14*. Springer, 2016, pp. 443–450.
- [31] G. Kang, L. Jiang, Y. Yang, and A. G. Hauptmann, “Contrastive adaptation network for unsupervised domain adaptation,” in *Proc. IEEE/CVF Conf. Comput. Vis. Pattern Recognit.*, 2019, pp. 4893–4902.
- [32] H. Ajakan *et al.*, “Domain-adversarial neural networks,” *arXiv preprint arXiv:1412.4446*, 2014.
- [33] K. A. Zhang, A. Cuesta-Infante, L. Xu, and K. Veeramachaneni, “Steganogan: High capacity image steganography with gans,” *arXiv preprint arXiv:1901.03892*, 2019.
- [34] H. Zhao, C. Ma, Q. Chen, and Z.-H. Deng, “Domain adaptation via maximizing surrogate mutual information,” *arXiv preprint arXiv:2110.12184*, 2021.
- [35] J. Guo *et al.*, “Domain watermark: Effective and harmless dataset copyright protection is closed at hand,” *Proc. Adv. Neural Inform. Process. Syst.*, vol. 36, 2024.
- [36] P. Cheng *et al.*, “Club: A contrastive log-ratio upper bound of mutual information,” in *Proc. Int. Conf. Mach. Learn.* PMLR, 2020, pp. 1779–1788.
- [37] R. A. Jacobs *et al.*, “Adaptive mixtures of local experts,” *Neural Comput.*, vol. 3, no. 1, pp. 79–87, 1991.
- [38] L. Van der Maaten and G. Hinton, “Visualizing data using t-sne,” *J. Mach. Learn. Res.*, vol. 9, no. 11, 2008.
- [39] Y. Li *et al.*, “Neural attention distillation: Erasing backdoor triggers from deep neural networks,” *arXiv preprint arXiv:2101.05930*, 2021.
- [40] S. Zagoruyko and N. Komodakis, “Paying more attention to attention: Improving the performance of convolutional neural networks via attention transfer,” *arXiv preprint arXiv:1612.03928*, 2016.
- [41] Y. Tian, D. Krishnan, and P. Isola, “Contrastive representation distillation,” *arXiv preprint arXiv:1910.10699*, 2019.
- [42] A. Krizhevsky and G. Hinton, “Learning multiple layers of features from tiny images,” 2009.
- [43] S. Houben, J. Stallkamp, J. Salmen, M. Schlipsing, and C. Igel, “Detection of traffic signs in real-world images: The German Traffic Sign Detection Benchmark,” in *Proc. Int. Joint Conf. Neural Networks*, no. 1288, 2013.
- [44] L. Fei-Fei, R. Fergus, and P. Perona, “Learning generative visual models from few training examples: An incremental bayesian approach tested on 101 object categories,” *Comput. Vision Pattern Recognit. Workshop*, 2004.
- [45] J. Deng *et al.*, “Imagenet: A large-scale hierarchical image database,” in *Proc. IEEE Conf. Comput. Vis. Pattern Recognit.* Ieee, 2009, pp. 248–255.
- [46] K. He, X. Zhang, S. Ren, and J. Sun, “Deep residual learning for image recognition,” in *Proc. IEEE Conf. Comput. Vis. Pattern Recognit.*, 2016, pp. 770–778.
- [47] J. Hu, L. Shen, and G. Sun, “Squeeze-and-excitation networks,” in *Proc. IEEE Conf. Comput. Vis. Pattern Recognit.*, 2018, pp. 7132–7141.
- [48] A. G. Howard *et al.*, “Mobilenets: Efficient convolutional neural networks for mobile vision applications,” *arXiv preprint arXiv:1704.04861*, 2017.
- [49] A. Hore and D. Ziou, “Image quality metrics: Psnr vs. ssim,” in *Proc. Int. Conf. Pattern Recognit.* IEEE, 2010, pp. 2366–2369.
- [50] R. Zhang *et al.*, “The unreasonable effectiveness of deep features as a perceptual metric,” in *Proc. IEEE Conf. Comput. Vis. Pattern Recognit.*, 2018, pp. 586–595.
- [51] Y. Chen, J. Tian, X. Chen, and J. Zhou, “Effective ambiguity attack against passport-based dnn intellectual property protection schemes through fully connected layer substitution,” in *Proc. IEEE/CVF Conf. Comput. Vis. Pattern Recognit.*, 2023, pp. 8123–8132.
- [52] N. Lukas, E. Jiang, X. Li, and F. Kerschbaum, “Sok: How robust is image classification deep neural network watermarking?” in *Proc. IEEE Symp. Secur. Privacy.* IEEE, 2022, pp. 787–804.
- [53] S. Han, J. Pool, J. Tran, and W. Dally, “Learning both weights and connections for efficient neural network,” vol. 28, 2015.
- [54] K. Liu, B. Dolan-Gavitt, and S. Garg, “Fine-pruning: Defending against backdooring attacks on deep neural networks,” in *Proc. Int. Symp. Res. Attacks, Intrusions, Defenses.* Springer, 2018, pp. 273–294.